The Astrophysical Journal, 951:26 (15pp), 2023 July 1 https://doi.org/10.3847/1538-4357/accf13

Distant Echoes of the Milky Way's Last Major Merger

Vedant Chandra[1], Rohan P. Naidu[1,2,10], Charlie Conroy[1], Alexander P. Ji[3,4], Hans-Walter Rix[5], Ana Bonaca[6], Phillip A. Cargile[1], Jiwon Jesse Han[1], Benjamin D. Johnson[1], Yuan-Sen Ting (丁源森)[7,8], Turner Woody[1], and Dennis Zaritsky[9]

[1] Center for Astrophysics | Harvard & Smithsonian, 60 Garden Street, Cambridge, MA 02138, USA; vedant.chandra@cfa.harvard.edu
[2] MIT Kavli Institute for Astrophysics and Space Research, 77 Massachusetts Avenue, Cambridge, MA 02139, USA
[3] Department of Astronomy & Astrophysics, University of Chicago, 5640 S Ellis Avenue, Chicago, IL 60637, USA
[4] Kavli Institute for Cosmological Physics, University of Chicago, Chicago, IL 60637, USA
[5] Max-Planck-Institut für Astronomie, Königstuhl 17, D-69117 Heidelberg, Germany
[6] The Observatories of the Carnegie Institution for Science, 813 Santa Barbara Street, Pasadena, CA 91101, USA
[7] Research School of Astronomy & Astrophysics, Australian National University, Cotter Road, Weston, ACT 2611, Australia
[8] School of Computing, Australian National University, Acton, ACT 2601, Australia
[9] Steward Observatory and Department of Astronomy, University of Arizona, Tucson, AZ 85721, USA

Received 2022 November 30; revised 2023 April 10; accepted 2023 April 19; published 2023 June 29

Abstract

The majority of the Milky Way's stellar halo consists of debris from our galaxy's last major merger, the Gaia-Sausage-Enceladus (GSE). In the past few years, stars from the GSE have been kinematically and chemically studied in the inner 30 kpc of our galaxy. However, simulations predict that accreted debris could lie at greater distances, forming substructures in the outer halo. Here we derive metallicities and distances using Gaia DR3 XP spectra for an all-sky sample of luminous red giant stars, and map the outer halo with kinematics and metallicities out to 100 kpc. We obtain follow-up spectra of stars in two strong overdensities—including the previously identified outer Virgo Overdensity—and find them to be relatively metal rich and on predominantly retrograde orbits, matching predictions from simulations of the GSE merger. We argue that these are apocentric shells of GSE debris, forming 60–90 kpc counterparts to the 15–20 kpc shells that are known to dominate the inner stellar halo. Extending our search across the sky with literature radial velocities, we find evidence for a coherent stream of retrograde stars encircling the Milky Way from 50 to 100 kpc, in the same plane as the Sagittarius Stream but moving in the opposite direction. These are the first discoveries of distant and structured imprints from the GSE merger, cementing the picture of an inclined and retrograde collision that built up our galaxy's stellar halo.

Unified Astronomy Thesaurus concepts: Milky Way stellar halo (1060); Stellar streams (2166); Galaxy mergers (608); Milky Way formation (1053); Milky Way Galaxy (1054)

1. Introduction

The majority of our galaxy's stellar halo was likely deposited by one massive merger event, the so-called Gaia-Sausage-Enceladus (GSE; e.g., Deason et al. 2013; Belokurov et al. 2018; Helmi et al. 2018). The GSE was discovered as a distinct sequence in the color–magnitude diagram (CMD) of halo stars and as a coherent kinematic population in memory-preserving integrals of motion. Subsequent work has developed a picture of a merger ≈8–10 Gyr ago that built up most of the present-day stellar halo (e.g., Haywood et al. 2018; Gallart et al. 2019; Mackereth et al. 2019; Gallart et al. 2019; Bignone et al. 2019; Fattahi et al. 2019; Lancaster et al. 2019; Vincenzo et al. 2019; Bonaca et al. 2020; Das et al. 2020; Naidu et al. 2020, 2021; Belokurov et al. 2023). To date, the GSE has been extensively studied in the inner halo of the Milky Way, out to ≈30 kpc. In this regime, the GSE debris are thoroughly phase mixed, and must be identified via kinematic or chemical signatures. Consequently, models are relatively unconstrained regarding the precise orientation and dynamics of the merger.

The hallmark of a major merger like the GSE is rapid radialization, depositing stars on radial orbits with low azimuthal angular momenta and high eccentricities (e.g., Amorisco 2017; N21; Vasiliev et al. 2022). The metallicity distribution function (MDF) of the GSE sharply peaks at $[\mathrm{Fe/H}] \approx -1.2$ and is well fit by a simple chemical evolution model (e.g., Feuillet et al. 2020; Hasselquist et al. 2020; Naidu et al. 2020; Horta et al. 2023; Johnson et al. 2022; Limberg et al. 2022). Naidu et al. (2020) report a population of retrograde stars dubbed "Arjuna" that closely matches this MDF, and argued that it may represent the early-stripped tail of GSE stars. The existence of this population hints at a retrograde orientation for the merger. Belokurov et al. (2023) instead argue for a prograde configuration based on a mild prograde tilt of nearby ($d \lesssim 15$ kpc) GSE debris in the Gaia DR3 Radial Velocity Survey (RVS) sample (Gaia Collaboration et al. 2022a; Katz et al. 2022). Linking the orientation of present-day inner debris to the original trajectory of the merger is further complicated by any precession of the Milky Way disk since $z \approx 2$, which would change the net angular momentum vector of the galaxy (e.g., Dillamore et al. 2022; Dodge et al. 2023).

Naidu et al. (2021; hereafter N21) ran a comprehensive suite of *N*-body simulations of the GSE merger, tailor-made to reproduce the kinematics of the GSE and Arjuna stars from the H3 Survey (Conroy et al. 2019b). Their fiducial model consists of an $M_* = 5 \times 10^8 \, M_\odot$ merger beginning at $z \approx 2$, which started out with a tilted and retrograde orientation before

---

[10] NASA Hubble Fellow.

rapidly radializing. No spatial constraints were used to orient their simulations—the initially retrograde orientation is required to reproduce Arjuna's kinematics in the H3 Survey (Naidu et al. 2020). Nonetheless, their model reproduces the spatial orientation of the observed stellar halo out to ≈40 kpc (Jurić et al. 2008; Xue et al. 2015; Das & Binney 2016; Iorio et al. 2018; Iorio & Belokurov 2019), including a primary axis tilted off the plane of the Galactic disk (Han et al. 2022) and aligned with the so-called Hercules–Aquila Cloud (HAC; Belokurov et al. 2007; Simion et al. 2018, 2019) and inner Virgo Overdensity (VO; Jurić et al. 2008; Bonaca et al. 2012; Donlon et al. 2019). Li et al. (2016) previously linked the orbit of the so-called Eridanus–Phoenix overdensity to the HAC and VO as well, suggesting a common origin for all three structures.

The HAC and VO define a preferred spatial axis for GSE debris between ≈10 and 20 kpc. One of the key predictions from N21 is a stellar stream of retrograde GSE stars beyond these distances, possessing a similar on-sky track to the Sagittarius Stream, albeit moving in the opposite direction. This debris should also contain observable apocentric overdensities, with stars "echoing" back and forth between regions of pileup on the sky. The prediction of debris beyond ≈50 kpc is generic to simulations of this merger, with more radially anisotropic configurations producing larger fractions of distant debris (e.g., Bignone et al. 2019; Elias et al. 2020).

At more than four times the distance from the GSE-associated VO lies the outer Virgo Overdensity (OVO; Sesar et al. 2017a), a hitherto mysterious structure discovered via RR Lyrae (RRL) stars at ≈80 kpc. It is interesting to consider that this outer overdensity lies in one of two preferred octants for debris from the GSE merger, perhaps linking it to the extended outer streams predicted by simulations. Likewise, Carlin et al. (2012) used orbital information to associate the VO to the southern Pisces Overdensity at ≈70 kpc, another possible distant remnant of the GSE (Sesar et al. 2007; Kollmeier et al. 2009; Sesar et al. 2010).

However, disentangling and interpreting these structures has thus far been challenging in the absence of kinematic information. Although RRL stars have long been standard outer halo tracers due to their precise distances, at 80 kpc they have typical Gaia DR3 tangential (proper motion) velocity uncertainties $\sigma_{\rm v} \approx 300$ km s^{-1}. It is also challenging to measure radial velocities for RRL stars since they exhibit pulsation phase-dependent RV variations that need to be modeled. This makes them unsuitable to search for cold velocity substructures in the outer halo, motivating the need for more luminous tracers like red giant stars.

Red giant branch (RGB) stars are luminous tracers with characteristic tangential velocity uncertainties $\sigma_{\rm v} \lesssim 30$ km s^{-1} at 80 kpc, an order of magnitude improvement over RRL stars. This comes at the cost of distance accuracy, and their isochrone distances particularly depend on the assumed metallicity. The third data release from Gaia has revolutionized this latter effort by releasing low-resolution ($R \approx 50$–100) "XP" prism spectra for $\gtrsim$200 million stars brighter than $G \lesssim 17.6$ (De Angeli et al. 2022; Montegriffo et al. 2023). These spectra enable us to measure metallicities for red giant stars, deriving much more accurate distances than previously possible. This data set enables us to, for the first time, map the outer halo comprehensively with 5D and—for the subset with follow-up and literature radial velocities—6D kinematic information.

In this work, we use luminous red giants with 5D and 6D kinematics to discover echoes of the GSE in the outer halo of the galaxy. We use Gaia DR3 astrometry and spectrophotometry to construct a pure sample of red giants out to 100 kpc. We augment this sample with radial velocities from follow-up spectra and existing spectroscopic surveys, creating an unprecedented data set with 6D kinematics in the outer halo. We describe our sample construction, metallicity measurements, and follow-up spectroscopy in Section 2. We present our analysis of apocentric overdensities in Section 3, and extend our search for GSE debris across the sky in Section 4. We conclude by discussing our results and future lines of inquiry in Section 5.

2. Data and Analysis

2.1. Selecting RGB Stars

We begin by assembling a sample of RGB stars using Gaia DR3 astrometry and unWISE infrared photometry (Mainzer et al. 2014; Schlafly et al. 2019; Brown et al. 2021; Lindegren et al. 2021; Gaia Collaboration et al. 2022a). We query Gaia DR3 for sources with $\varpi < 0.4$ mas, $\mu < 5$ mas yr^{-1}, and $|b| > 20°$ to remove obvious nearby dwarfs and mask out the Milky Way disk. Gaia parallaxes for distant giants are typically low-significance measurements that cannot reliably be turned into distances—most have $\varpi/\sigma_\varpi \lesssim 1$. However, these parallaxes are still powerful to remove contamination from foreground dwarf stars. For a star with a given apparent G magnitude and BP $-$ RP color, we predict the parallax of a $\log g = 4$ dwarf using MIST isochrones (Choi et al. 2016). We divide the difference between the predicted and observed parallax by the predicted parallax uncertainty for the star's G magnitude, deriving a significance statistic χ_ϖ that encodes how many standard deviations lie between the observed parallax and the prediction for a dwarf. Using stars from the H3 Spectroscopic Survey (Conroy et al. 2019b) as a guide, we find that removing stars with $\chi_\varpi < 2$ results in a ≈90% pure sample of stars with $\log g < 3.5$.

We further purify this sample by applying a broad color cut in the (BP − RP, RP − W1) color space to remove dwarfs based on their WISE infrared colors (Conroy et al. 2018, 2021), which increases the sample purity to $\gtrsim$95%. Our resulting parent sample consists of ≈200,000 RGB stars brighter than $G \leqslant 17.65$ in the color range $1.3 \leqslant {\rm BP} - {\rm RP} \leqslant 3$, i.e., K- and M-type giants.

2.2. 5D Giants: Metallicities and Distances with Gaia XP

Mapping the spatial and orbital properties of giants requires an estimate of their distance, and photometric isochrone distances are heavily dependent on the assumed metallicity (e.g., Conroy et al. 2021). We therefore derive spectrophotometric metallicities for our giants using low-resolution "XP" prism spectra from Gaia DR3 (De Angeli et al. 2022; Montegriffo et al. 2023). In order to compress the information contained in these continuously represented spectra into astrophysically interpretable quantities, we compute integrated photometry in several narrowband filters using the `GaiaXPy` utility (v1.0.2; Gaia Collaboration et al. 2022b; Ruz-Mieres 2022). These filters are drawn from the J-PLUS and Strömgren systems, and are centered on absorption features that are sensitive to stellar parameters like metallicity (Figure 1; see, e.g., Strömgren 1966; Bailer-Jones 2004; Marín-Franch et al. 2012). As our feature set, we use colors of

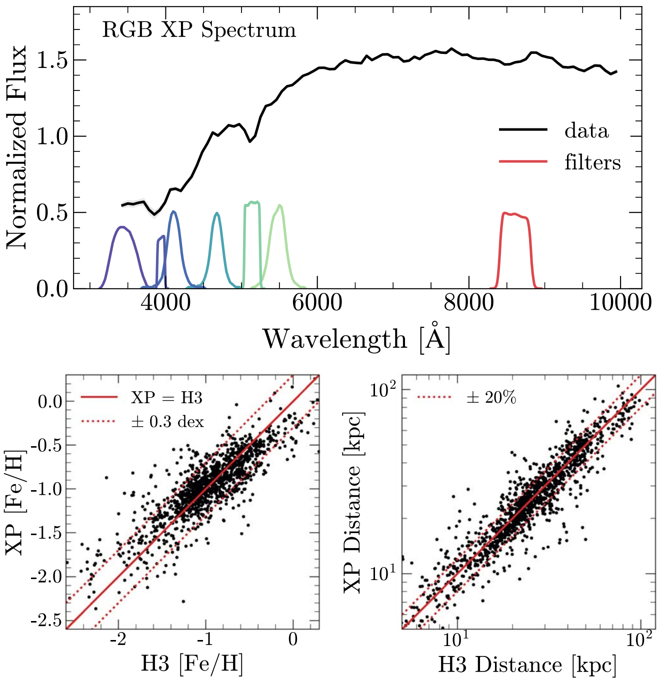

Figure 1. Top: example of an observed Gaia DR3 XP spectrum of an RGB star. We display the medium-band photometric filters—Strömgren with round peaks, J-PLUS with flat peaks—for which we synthesize photometry from these spectra, in order to predict their metallicities and distances. Bottom: validating our XP-derived metallicities and distances by comparing against spectroscopic measurements from the H3 Survey. We use two-fold cross-validation here, i.e., we train the model on half the data and evaluate it on the other half, and vice versa.

the following bands relative to the synthesized g band: J0395, J0515, J0861, u, v, b, and y. We deredden these colors using the dust maps of Schlegel et al. (1998)—renormalized by Schlafly & Finkbeiner (2011)—and restrict our sample to $E(B-V) \leqslant 0.3$. In practice this removes a small fraction of our sample, since most high-extinction regions are already masked out via the $|b| > 20°$ cut on the parent sample.

To map this multidimensional feature set to metallicities, we use high-resolution spectroscopic data from the H3 Survey (Conroy et al. 2019b), which have metallicities estimated using the `MINESweeper` routine (Cargile et al. 2020). Ideally, we would build a generative model of the spectral energy distributions using theoretical spectra and estimate metallicities in a full fitting framework. However, this method is sensitive to offsets between the theoretical and observed colors, which are challenging to isolate and correct. Instead, we opt for a discriminative regression in which we directly map colors to metallicities in observed space. This circumvents systematic offsets in the theoretical models or filter curves, at the cost of a well-defined error model for the predicted metallicities. This trade-off is quite justified for our present science case (see Rix et al. 2023 for an application of similar techniques).

We select ≈1500 stars from our parent sample that were also observed by the H3 Survey, and consequently have high-resolution [Fe/H] measurements. These stars span a wide range of parameters: $3800 \lesssim T_{\rm eff}/{\rm K} \lesssim 5000$, $0 \lesssim \log g \lesssim 4$, and $-3.0 \lesssim [{\rm Fe/H}] \lesssim 0.3$. We train a two-layer neural network with 16 neurons in each layer to map our XP-synthesized color space to the H3-measured [Fe/H] and $\log g$ (Pedregosa et al. 2011). We experimented with less flexible models like linear and quadratic regression, and found that the neural network produced a noticeably better rms prediction error on the test data that was withheld from the training set. We use two-fold cross-validation—training on 1/2 of our data set and predicted on the remaining 1/2, and vice versa—to increase our confidence that the chosen regression model is not overfitting the training data. Our final model predicts H3 [Fe/H] to within 0.3 dex on average, and $\log g$ to within 0.1 dex, with negligible bias (Figure 1, bottom left). Due to the purity of our parent giant sample the vast majority of the data have XP-inferred $\log g < 3.5$, but we use the $\log g$ predicted by our model to clean the sample further and remove nongiants with XP-predicted $\log g > 3.5$ (≈1% of the stars).

We estimate G-band distance moduli—and consequently distances—to all ≈200,000 giants in our sample using a 10 Gyr MIST isochrone spline-interpolated to each star's XP-inferred [Fe/H] and $\log g$. This assumption of a fixed age is well founded (e.g., Bonaca et al. 2020), and a factor of two change in the assumed age affects the resulting distances by less than 10%. A comparison to spectroscopic distances from the H3 Survey demonstrates that we obtain unbiased distances with $\lesssim$20% scatter out to 100 kpc (Figure 1, bottom right).

2.3. 6D Giants

2.3.1. Literature Radial Velocities

In order to derive 6D phase-space information for a subset of our sample, we cross-match our giants to catalogs from the Sloan Extension for Galactic Understanding and Exploration (SEGUE; Lee et al. 2008; Yanny et al. 2009; Eisenstein et al. 2011; Alam et al. 2015), and Large Sky Area Multi-Object Fiber Spectroscopic Telescope (LAMOST; Cui et al. 2012; Zhao et al. 2012; Xiang et al. 2019), as well as the H3 Survey (Conroy et al. 2019b; Cargile et al. 2020). We use a version of the SEGUE catalog with parameters estimated via the `MINESweeper` routine (Cargile et al. 2020), which should have more robust [α/Fe] values than the default pipeline, and includes spectrophotometric distances. We do not utilize the Gaia DR3 RVS (Katz et al. 2022) here, since it contains near-zero stars beyond 50 kpc due to its shallow depth. This yields ≈12,000 giants with 6D kinematic information and spectroscopic metallicities, ≈1100 of which are beyond 40 kpc. We refer to both the "5D giant" and "6D giant" data sets in this paper.

2.3.2. Follow-up Spectroscopy with MIKE

To sample the two outer halo overdensities studied in this work more comprehensively, we obtained follow-up spectroscopy for 29 XP-selected giants using the Magellan Inamori Kyocera Echelle (MIKE; Bernstein et al. 2003) spectrograph on the 6.5 m Magellan Clay telescope at Los Campanas Observatory in Chile (PIs Naidu and Ji). We used ≈10 minutes exposures with the $0\farcs7$ slit to attain a signal-to-noise ratio (S/N) $\gtrsim$10 on the red end of the $R \approx 20{,}000$ spectra. We reduced the data using the CarPy utility, and derived radial velocities using Payne4MIKE with typical uncertainties ≈0.5 km s^{-1} (Kelson 2003; Ting et al. 2019, A. P. Ji et al. 2023, in preparation). Further details on the target selection and analysis are described in Section 3.

Our MIKE spectra have SNR ≈10 in the calcium triplet (CaT) region, but only S/N ≈ 1 in the bluer (≈5000 Å) portions of the spectrum, hampering a sophisticated fit to the entire optical spectrum. We therefore derive metallicities for our MIKE stars using the CaT calibration of Carrera et al. (2013). We fit Voigt profiles to each of the three CaT absorption lines using `lmfit` (Newberg et al. 2009) and derive their equivalent widths. The Carrera et al. (2013) calibration relies on the summed equivalent widths and absolute V-band luminosity (M_V) of the star. We make a first estimate of M_V using the XP-inferred metallicity and MIST isochrones. We then compute the spectroscopic metallicity following Carrera et al. (2013), and recompute M_V. This process is iterated until the metallicity and M_V converge, which in practice occurs within five iterations.

Our MIKE CaT metallicities are broadly consistent with the XP metallicities for these stars, with a median absolute deviation of ≈0.2 dex and a bias of ≈−0.1 dex, and with the MIKE metallicities being slightly more metal poor than the XP ones (recall that the XP metallicities were trained on H3 Survey data, Section 2.2). This offset is unsurprising given that our adopted CaT metallicity calibration does not take into account α-enhancement, whereas H3 jointly fits for [Fe/H] and [α/Fe] with high-resolution spectra of the Mgb triplet region (Cargile et al. 2020). We utilize the MIKE metallicities (and their corresponding isochrone distances) for the remainder of this work except where otherwise noted, while cautioning that there is a slight offset in the MIKE metallicity scale compared to XP and the H3 Survey.

2.3.3. Orbital Parameters

We compute orbital parameters for stars with 6D phase-space information using `gala` (Price-Whelan 2017; Price-Whelan et al. 2020), adopting the default `MilkyWayPotential`. For the solar position with respect to the galaxy, we adopt radius $r_\odot = 8.122$ kpc (GRAVITY Collaboration et al. 2018), and height above the midplane $z_\odot = 20.8$ pc (Bennett & Bovy 2019). We use a right-handed Galactocentric Cartesian coordinate frame with solar position $\boldsymbol{x}_\odot = (-8.12, 0.00, 0.02)$ kpc, and solar velocity $\boldsymbol{v}_\odot = (12.9, 245.6, 7.8)$ km s^{-1} (Reid & Brunthaler 2004; Drimmel & Poggio 2018; GRAVITY Collaboration et al. 2018). Orbital parameters are computed after numerically integrating the orbits with a time step of 1 Myr over 2.5 Gyr.

3. Apocenter Pileup: Echoes in the Galactic North and South

In this section, we use our Gaia DR3 sample to identify RGB stars in the OVO and Pisces Overdensity, and characterize their kinematics and chemistry with follow-up MIKE spectroscopy. We argue that these overdensities represent apocentric shells from the GSE merger, matching several key predictions from simulations of the merger. Finally, we use these stars—along with the N21 simulations—to measure the metallicity gradient of the GSE progenitor out to the edge of its disk.

3.1. Spectroscopic Follow-up of the OVO and Its Southern Counterpart

Figure 2 illustrates the $d > 40$ kpc outer halo with ≈6600 RRL stars from Gaia DR3 (top panel; Clementini et al. 2022), and ≈8500 of our 5D XP RGB stars (bottom panel). Several key structures and overdensities are highlighted. The OVO was first identified by Sesar et al. (2017a) using RRL stars from Pan-STARRS (Sesar et al. 2017b). It was described as a strong excess of Pan-STARRS RRL stars clustered around $(\alpha, \delta) \approx (207, -7)$ at a distance of ≈80 kpc, with a line-of-sight Gaussian extent of ∼4 kpc (Chambers et al. 2016; Sesar et al. 2017a, 2017b). The northern map is dominated by the distant arm of Sagittarius (Majewski et al. 2003), whereas in the south the elongated Pisces Plume is prominent (Belokurov et al. 2019; Conroy et al. 2021). We overlay a polynomial track ±10° around $l = -60 + 0.1b + 0.007b^2$ to guide the eye along the Plume. The origin of the Pisces Plume is uncertain, particularly whether it contains debris stripped from the Magellanic Clouds, or if it mainly represents the dynamical friction wake of the Large Magellanic Cloud (Belokurov et al. 2019; Conroy et al. 2021).

Apart from the Plume, there is another prominent southern overdensity that we highlight in blue. This structure is spatially coincident with the previously identified Pisces Overdensity (Sesar et al. 2007; Kollmeier et al. 2009; Watkins et al. 2009; Nie et al. 2015), and like the OVO lies in one of the preferred octants for GSE debris. We delineate this structure with $60° < l < 140°$ and $-80° < b < -40°$, enclosing the previously identified regions of the overdensity. Our selection is significantly wider than past surveys of the Pisces Overdensity, since the overdensity in our K-giant sample spans a larger swath on the sky.

The OVO and Pisces Overdensity are shown in Galactic longitude–distance coordinates in Figure 3. We color the stars by their angular separation from the Sagittarius Stream track (Law & Majewski 2010a). The OVO stands out as a clear overdensity off the plane of Sagittarius, and at almost twice the distance of Sagittarius debris in the plane of the sky. The corresponding southern overdensity is weaker and more extended. However, previously identified RRL stars are insufficient to disentangle and identify populations kinematically due to their faintness and consequently large tangential velocity uncertainties. We therefore set out to obtain follow-up spectroscopy of RGB stars in both overdensities to obtain 6D kinematics and more precise metallicities for a representative sample of stars.

In the north, we selected 13 stars from our 5D XP giants data set that lie within ≈5° of the OVO with XP-inferred distances of ≈70–100 kpc, bracketing the OVO RRL stars. We applied no selections on the XP-inferred metallicity and kinematics for this northern sample. We performed a corresponding selection for 16 stars in the south, guided by the overdensity of stars visible in the all-sky RRL and RGB star maps (Figures 2 and 3). Since the southern overdensity is weaker and more extended, we applied selection in solar reflex-corrected proper motions of $\mu_\alpha^* > 0$ mas yr^{-1} (≈50% of the sample) to increase the likelihood of selecting retrograde stars. This was guided by the fact that there were two giants in our 6D RGB star catalog (with literature radial velocities) lying in the OVO, and both had retrograde kinematics. We therefore targeted stars with similar kinematics in the south, to ascertain if there was an associated population there. We account for this selection bias in the subsequent interpretations.

Our spectroscopic targets are shown in Galactic coordinates in Figure 2, and are also overlaid on the distance maps of Figure 3. The bottom panel of Figure 3 demonstrates that although our southern targets are in a similar region of sky as the previously identified Pisces Overdensity, they are closer and more extended in Galactic longitude. We henceforth refer to the respective MIKE samples as MIKE-N (northern OVO) and MIKE-S (southern counterpart around the Pisces

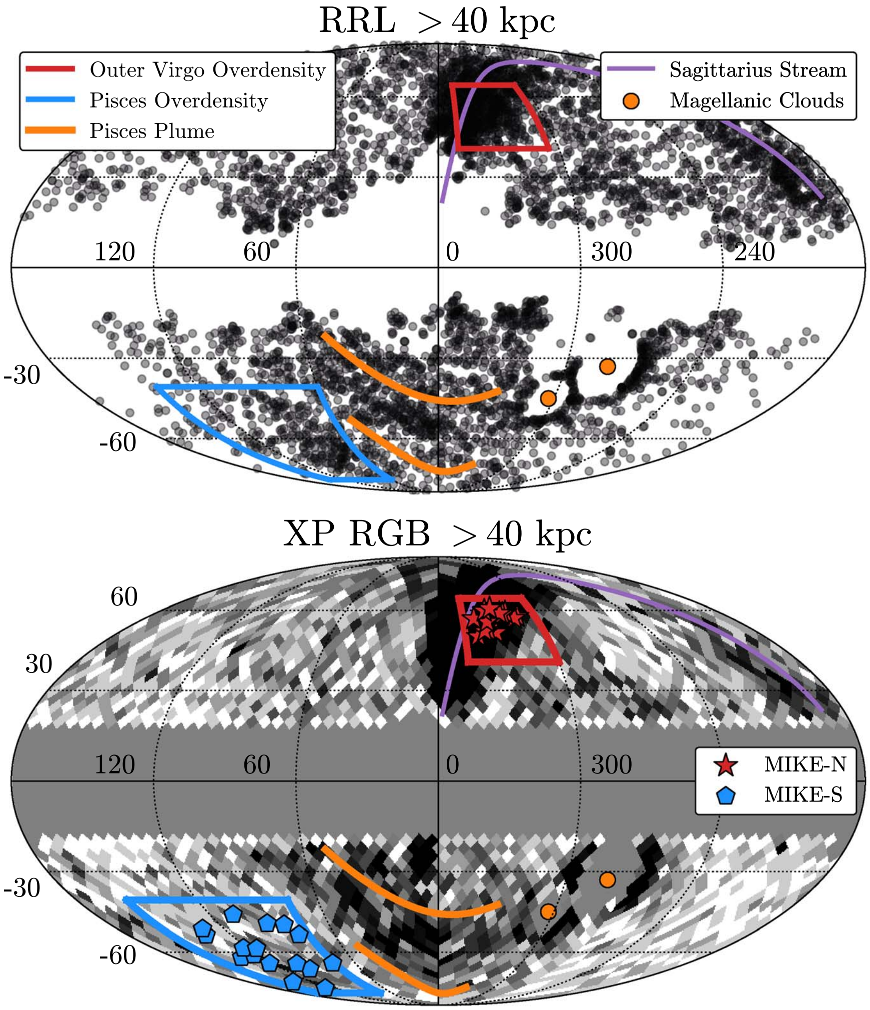

Figure 2. The spatial distribution of outer halo substructure as seen by RRL and RGB stars. Top: all-sky distribution of Gaia DR3 RRL stars beyond 40 kpc, with the overdensities studied in this work highlighted by red and blue boxes. Bottom: density distribution of our all-sky Gaia XP sample of RGB stars beyond 40 kpc. We overlay our spectroscopic targets in the MIKE-North (OVO) and MIKE-South (Pisces Overdensity) regions. There are observed overdensities of RRL and RGB stars in both these locations, albeit weaker and more extended in the south.

Overdensity) to avoid ambiguity. MIKE-N is an unbiased survey of stars lying in the OVO whereas MIKE-S is a proper motion-targeted search for stars near the Pisces Overdensity that have a higher likelihood of being retrograde.

3.2. Kinematics of the Outer Overdensities

Following the spectroscopic reduction and fitting described in Section 2.3.2, we are armed with 6D kinematics and chemistry for our MIKE targets. The MIKE-N stars have median MIKE (XP) $[\mathrm{Fe/H}] \approx -1.45$ (-1.31), whereas the MIKE-S stars have median MIKE (XP) $[\mathrm{Fe/H}] \approx -1.36$ (-1.28). This relatively high metallicity already points to a massive progenitor galaxy for these stars—in the outer halo, the two most likely sources of metal-rich stars are the GSE or Sagittarius. We note that Watkins et al. (2009) found a slightly lower $[\mathrm{Fe/H}] \approx -1.5$ in the Pisces Overdensity (MIKE-S) region, although their sample was more spatially concentrated and centered around 85 kpc compared to our broader sample around 60 kpc (see the bottom panel of Figure 3).

Conroy et al. (2019a) find that stars in the H3 Survey beyond 30 kpc have a richly structured metallicity distribution, with both metal-rich ($[\mathrm{Fe/H}] \approx -1.2$) and metal-poor ($[\mathrm{Fe/H}] \approx -2.0$) components. Subsequent work has argued that the majority of the $[\mathrm{Fe/H}] \approx -1.2$ stars can be attributed to the GSE merger (Naidu et al. 2020, 2021). Therefore, the metallicities of these overdensities suggest that they might share a common origin with the bulk of the field halo stars at these distances. GSE stars are expected to be tidally stripped over a range of radii, plausibly populating both the field halo and the apocentric overdensities presented in this work.

Figure 4 illustrates the kinematics of our MIKE sample. The inverse-variance weighted mean 6D phase-space coordinates of MIKE-N (MIKE-S) stars are integrated forward (backward) in time for 1 Gyr in the `gala` `MilkyWayPotential` with 1 Myr time steps. The motivation for these respective timescales is that in the N21 simulations, the northern debris temporally precede the southern debris as the GSE progenitor falls into the Milky Way. We sample the mean phase-space coordinates from their uncertainty distributions (assuming Gaussian uncertainties on the observed coordinates and kinematics) and display 100 realizations of these orbits in the top panel of Figure 4. The MIKE-N and MIKE-S populations—and by extension the underlying OVO and at least the retrograde portion of the Pisces Overdensity—appear kinematically associated, moving in a common orbital plane. The correspondence is not exact, suggesting that these populations

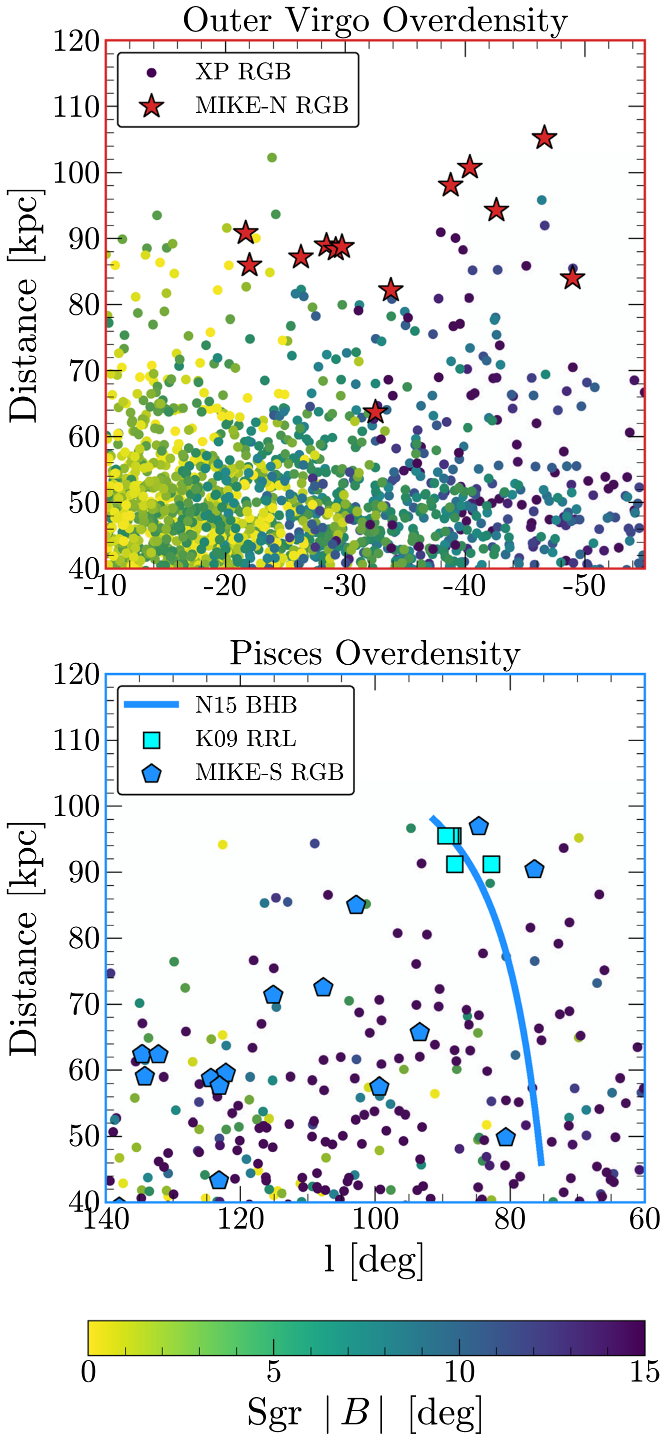

Figure 3. The Galactic longitude–distance distributions of XP RGB stars beyond 40 kpc in the OVO (top panel) and Pisces Overdensity (bottom panel) selection boxes shown in the all-sky maps of Figure 2. The OVO appears in the top panel as a distinct cloud of stars at ≈80 kpc, offset by ≈10° from the Sagittarius plane. The Pisces Overdensity RRL stars reported by Kollmeier et al. (2009) are overlaid in the bottom panel, along with the blue horizontal branch distance gradient measured by Nie et al. (2015). In both panels we overlay our MIKE targets using their spectroscopic distances.

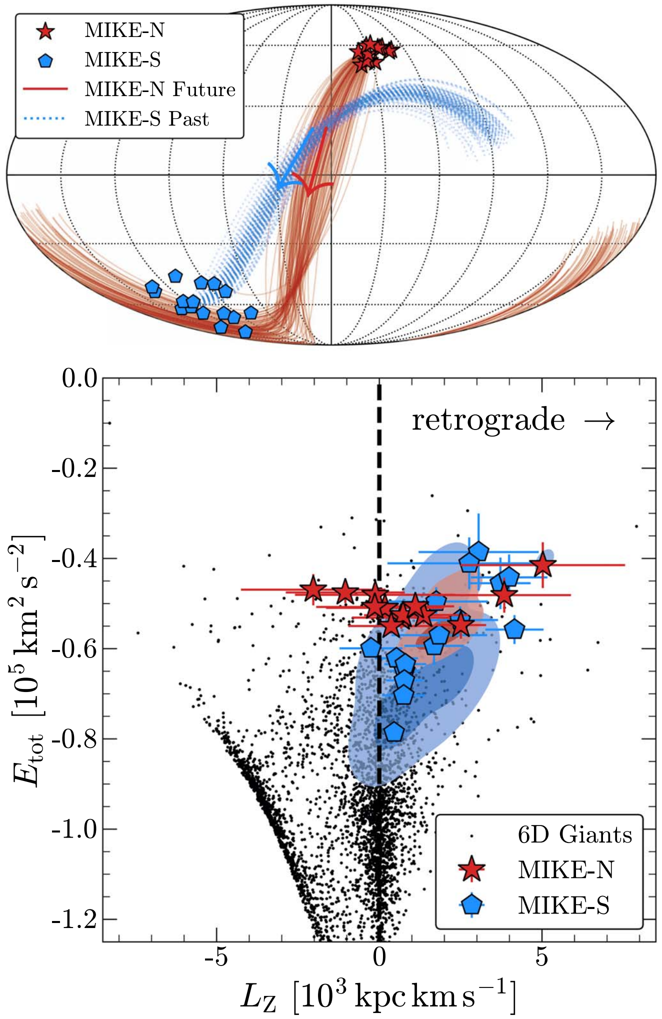

Figure 4. Top: future (past) orbits for the MIKE-N (MIKE-S) stars targeted in the OVO (Pisces Overdensity), integrated over 1 Gyr with arrows denoting the general direction of these orbits on sky. Bottom: MIKE targets in L_Z–$E_{\rm tot}$ space, with the Gaia XP 6D giant sample shown for comparison (black dots). The density distributions for N21 GSE simulation particles selected from analogous sky regions are shown using contours with corresponding colors. The MIKE stars in both hemispheres are overwhelmingly retrograde. Note that that the MIKE-S stars had a proper motion selection criterion that boosts the likelihood of being retrograde, whereas the MIKE-N stars were blindly targeted within the OVO (Section 3.1).

may have been stripped at different times during the merger, and hence occupy slightly different orbital planes and phases. Furthermore, the assumed potential is static and likely inaccurate in detail (e.g., Erkal et al. 2019; Koposov et al. 2023). Regardless, these orbits suggest that the northern stars will occupy a region near the southern overdensity in approximately a gigayear, and conversely that the southern stars used to reside near the northern overdensity approximately a gigayear ago. These are possible signatures of a pair of apocentric pileups, evoking an image of stars “echoing” between these overdensities over time.

The bottom panel of Figure 4 shows the azimuthal angular momentum versus total orbital energy of these stars. Stars targeted in the northern OVO are overwhelmingly retrograde, despite being selected without any kinematic bias. The two stars with slightly prograde kinematics could be interlopers from the nearby Sagittarius Stream, as they also have modestly negative L_Y (see the top panel of Figure 3). The southern stars were kinematically selected to have a high likelihood of being retrograde on the basis of proper motions, and are indeed all so. The retrograde nature of these stars strongly argues against an association with the Sagittarius Stream, which is highly prograde. These stars are also inconsistent with the extremely negative $L_{\rm Y}$ angular momentum of Sagittarius, having a median $L_{\rm Y} \approx 1 \times 10^3$ kpc km s^{-1}.

For comparison, we select star particles from the fiducial N21 GSE merger simulations lying in analogous northern and southern regions beyond ≈40 kpc, and overlay their distribution with contours in Figure 4. There is a reasonable correspondence between the models and data. In particular, the models predict that the southern stars lie at lower energies (smaller apocenters) than the northern stars, which is reflected in our data. Our MIKE-N targets have a median distance ≈80 kpc, whereas the MIKE-S stars lie ≈60 kpc away.

We estimate how close these stars are to their apocenters with the statistic $f_{\rm apo} = (r_{\rm gal} - r_{\rm peri})/(r_{\rm apo} - r_{\rm peri})$. The stars have a median $f_{\rm apo} \approx 0.94$ in the north and $f_{\rm apo} \approx 0.90$ in the south. This affirms our conclusion that these stars are piling up near their apocenters. This is analogous to our current understanding of the inner VO and HAC, which are likewise thought to consist of GSE stars near the apocenter (Iorio & Belokurov 2019; Simion et al. 2019; N21; Han et al. 2022; Perottoni et al. 2022).

Previously, Zaritsky et al. (2020) used data from the H3 Survey independently to identify a kinematically cold structure of 15 stars near the Pisces Overdensity at $40 \lesssim d/{\rm kpc} \lesssim 80$. This structure lies near our MIKE-S sample, although the Zaritsky et al. (2020) stars are more clustered around the canonical Pisces Overdensity highlighted by RRL stars than our more extended MIKE-S selection. They argued that these stars may be debris stripped from the Small Magellanic Cloud, based on their negative Galactocentric radial velocities and $[{\rm Fe/H}] \approx -1.4$ mean metallicity. Furthermore, the stars are linked in position and velocity with the gaseous Magellanic stream (Nidever et al. 2008).

As noted by Zaritsky et al. (2020), the distances and angular momenta of these stars are somewhat discrepant compared to the bulk of simulated Small Magellanic Cloud debris from Besla et al. (2013), although more recent simulations may be in better agreement (Lucchini et al. 2021). The structure reported by Zaritsky et al. (2020) is in fact modestly retrograde, and overlaps with the MIKE-S stars in orbital energy and between $L_{\rm Z} \approx 0$ and 1.5×10^3 kpc km s^{-1} (see Figure 4). We therefore speculate that the stars identified by Zaritsky et al. (2020) may also be associated with the distant GSE debris discovered in our work, with correspondence on sky, in kinematics, and in mean metallicity. However, this region of sky requires more comprehensive spectroscopy to disentangle the various structures—chiefly the Pisces Overdensity and Pisces Plume (see Figure 2)—and ascertain whether these stars are more plausibly associated with the GSE or the Small Magellanic Cloud.

4. Distant Streams of the GSE

In Section 3 we presented follow-up spectroscopy of a pair of on-sky overdensities that correspond to the most prominent GSE debris piling up near apocenter. In this section, we extend the search for debris across the sky using our data set of RGB stars with 6D kinematics via a cross-match to literature radial velocities. We identify a population of retrograde stars beyond 40 kpc that seem to form a coherent track on the sky, aligned with the apocentric overdensities described in Section 3. We suggest that these stars are likewise structured remnants from the merger, matching expectations of the GSE based on their kinematics and chemistry.

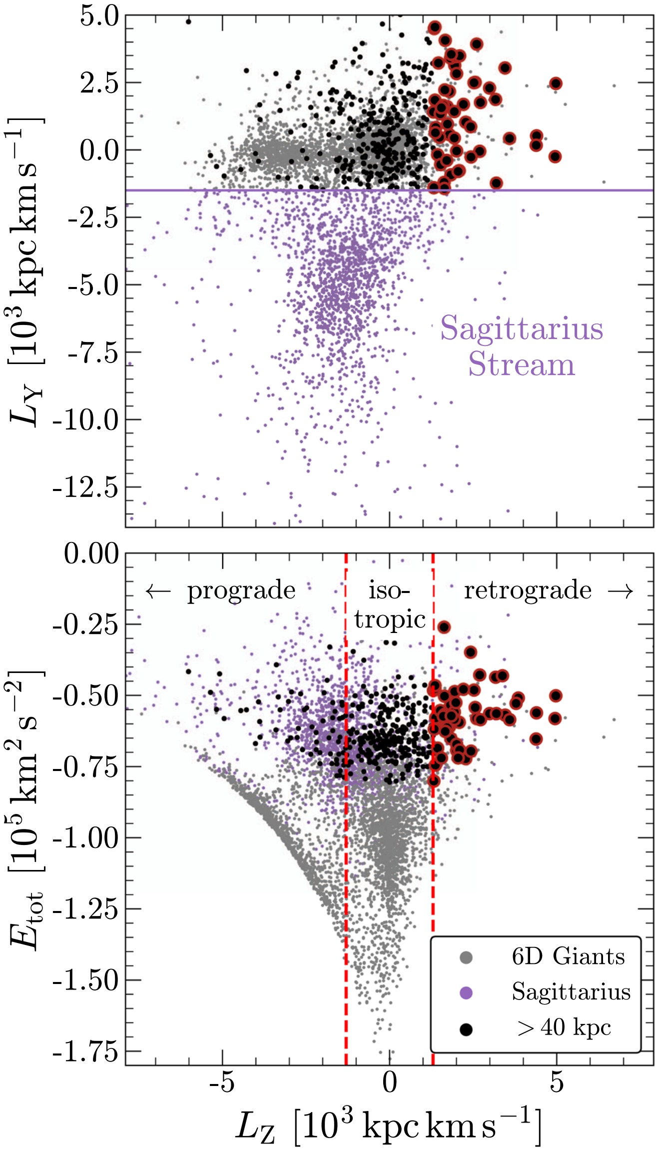

Figure 5. Isolating distant and retrograde debris in our 6D giant data set with literature radial velocities. Top: while members of the distant GSE debris and Sagittarius have considerable overlap in their $L_{\rm Z}$–$E_{\rm tot}$ distribution, they are quite distinct in the orientation of their orbital planes, reflected in $L_{\rm Y}$. This allows us to separate the Sagittarius Stream with with a simple $L_{\rm Y}$ cut, following Johnson et al. (2020). Bottom: the 6D giants in energy–angular momentum space, highlighting the distant $d > 40$ kpc subsample and separating stars into isotropic and retrograde bins, which are subsequently shown on sky in Figure 6.

4.1. Selection with 6D Giants

We begin with the 6D giant sample in the energy–angular momentum space (bottom panel of Figure 5). Three structures dominate this space: the prograde and rotationally supported disk, the eccentric and radial GSE locus around $L_{\rm Z} \approx 0$, and the cloud of Sagittarius Stream stars at higher energies. We disentangle and excise the Sagittarius stars using an $L_{\rm Y}$ cut following Johnson et al. (2020), coloring them separately in subsequent plots (Figure 5, top). Finally, we select stars with XP-inferred distances $d > 40$ kpc.

The resulting sample of distant stars is dominated by Sagittarius, with the remaining stars spanning a swath of azimuthal angular momenta. We split these stars into prograde, isotropic, and retrograde $L_{\rm Z}$ bins and display their spatial

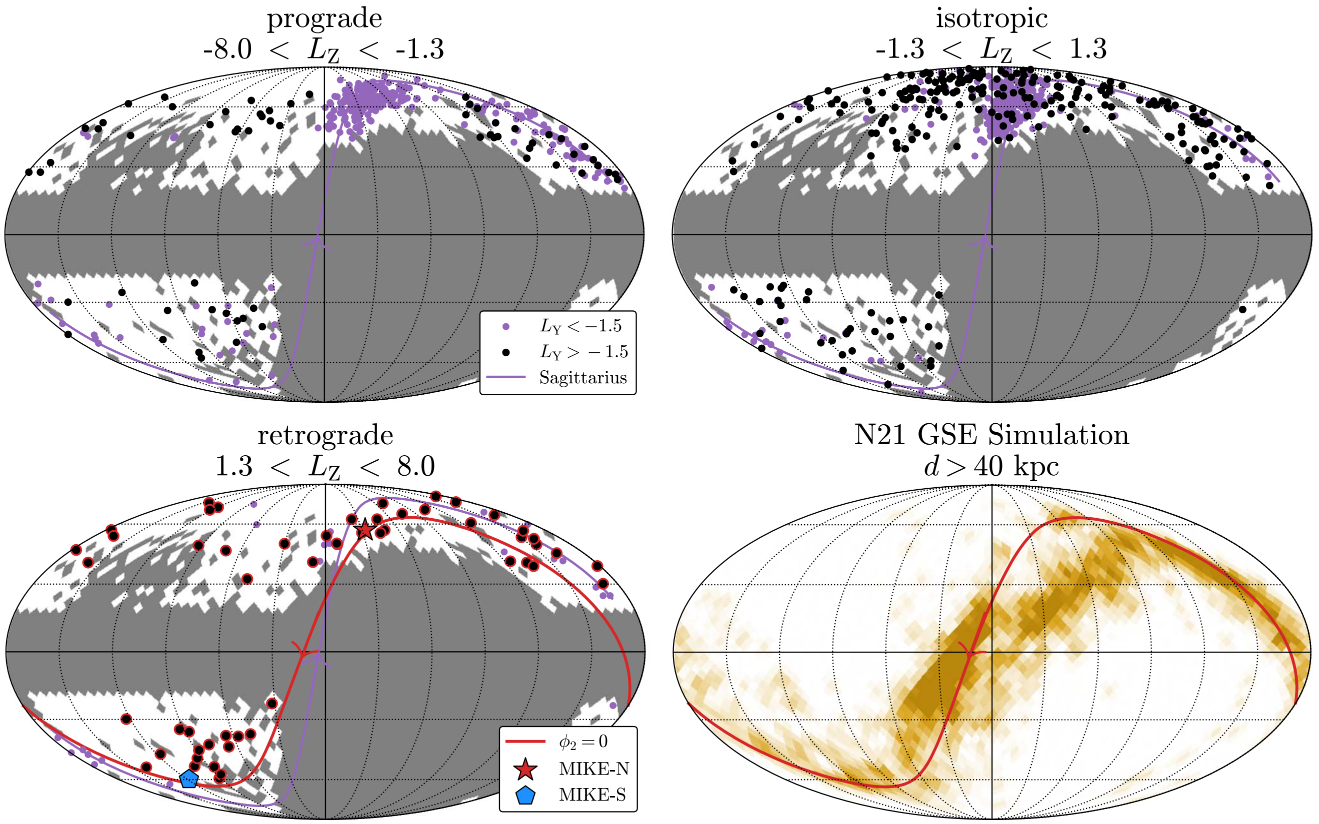

Figure 6. On-sky distribution of distant 6D giant stars, split into three subsets of azimuthal angular momentum L_Z in units of 10^3 kpc km s^{-1}: stars on prograde orbits, stars on isotropic orbits, and stars with retrograde orbits (see Figure 5). The selection function of the underlying spectroscopic surveys, and our Galactic latitude cut to mask out the Milky Way disk, is shaded in gray. Sagittarius Stream stars selected via L_Y are shown in purple. Whereas the stars with prograde and isotropic orbits are uniformly distributed across the survey footprints—apart from Sagittarius, which dominates these panels—the retrograde stars show a suggestive track on the sky, to which we fit the great circle shown in red. This track coincides with the MIKE-N (OVO) and MIKE-S (Pisces Overdensity) stars, whose median positions are overlaid. A red (purple) arrow indicates the on-sky orbital motion of the retrograde (Sagittarius) stars, emphasizing that the spatially overlapping debris move in opposite directions. In the bottom right panel we show GSE-only particles from the merger simulations of N21, selected to lie beyond 40 kpc.

distributions in Figure 6. The footprint of our underlying spectroscopic surveys is shown in white, whereas gray regions denote 13 deg^2 Healpixels containing zero spectra in the parent spectroscopic catalogs. The non-Sagittarius prograde stars are scattered across the sky (top left panel), although even our conservative L_Y cut appears to have missed some tightly clustered Sagittarius stars in the top right portion of the map. The bulk of Sagittarius stars fall into our isotropic L_Z bin (top right panel), with non-Sagittarius stars uniformly distributed across the sky. Finally, the retrograde selection entirely excludes the Sagittarius Stream based on kinematics (bottom left panel). Compared to the isotropic stars, the retrograde stars suggest a stream-like structure in the distant halo, aligned with the MIKE-N and MIKE-S samples presented in Section 3. These stars lie in a plane similar to that of the Sagittarius Stream, but move in the opposite direction. The appearance of this structure is certainly confounded by the selection footprint of the underlying (northern) spectroscopic surveys, although even just the northern $b \gtrsim 20^\circ$ stars exhibit a spatial asymmetry in the retrograde selection compared to the isotropic one. There is likely dominant GSE debris in both these panels, since even beyond 50 kpc about half of the GSE debris are predicted by N21 to be radial with low angular momenta. However, we focus here on the retrograde population because it can be clearly differentiated from the field stellar halo.

To quantify the orbital plane of this structure, we fit the distribution of retrograde stars with a great circle, minimizing the mean squared angular deviation of these stars from the great circle track. We use this fitted track to define a coordinate frame (ϕ_1, ϕ_2) aligned with the great circle (red line in the bottom panels of Figure 6). The overlaid track visually emphasizes how this sample of kinematically selected stars forms a coherent track on the sky, passing through the OVO and Pisces Overdensity. This structure has likely escaped detection thus far due to its spatial overlap with the Sagittarius Stream, which dominates these regions of the sky. Of the 6D giants beyond 40 kpc, ≈60% belong to the Sagittarius Stream selection in L_Y, whereas only ≈7% belong to the retrograde structure identified here.

We qualitatively compare our result with simulation-based predictions from N21 in the bottom right panel of Figure 6. We perform the same $d > 40$ kpc selection as the data and display the on-sky density of simulated star particles, overlaying the fitted track described above. We emphasize here that the N21 simulations did not utilize any spatial information to constrain their model, yet the predicted track of distant GSE debris is quite consistent with our data. This lends further credence to the proposed retrograde orientation of the merger, building on prior evidence that the GSE produced the $d \approx 20$ kpc HAC and (inner) VO (Simion et al. 2019; Perottoni et al. 2022).

4.2. Stream Coordinates and Chemistry

Figure 7 illustrates our sample in the transformed great circle (ϕ_1, ϕ_2) coordinate frame. The entire distant 6D giant sample is

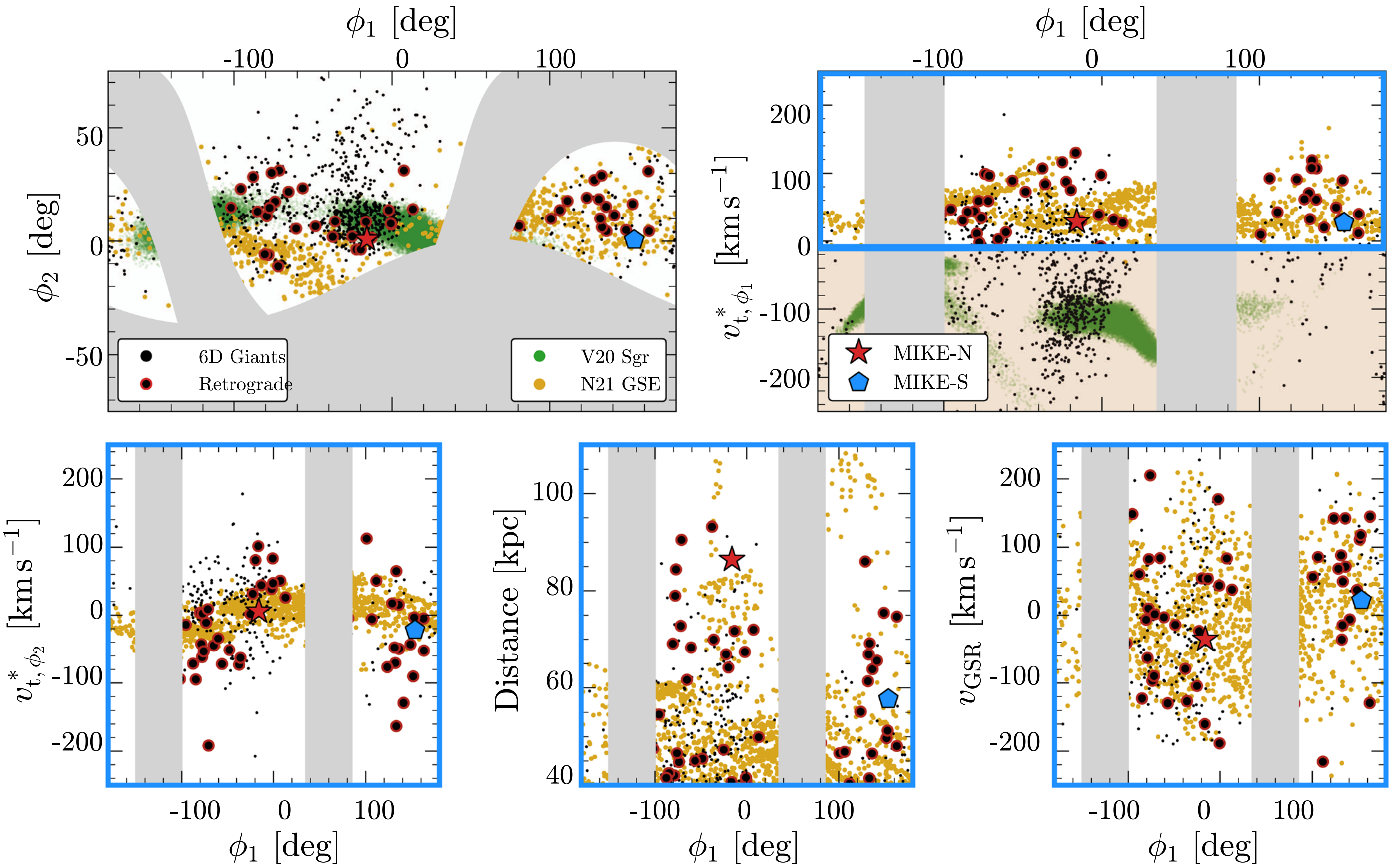

Figure 7. Comparison of the distant debris identified in this work to simulations of the GSE and Sagittarius, shown in the transformed great circle coordinate frame. We show all distant 6D giants from our sample in black, and retrograde giants are outlined in red. GSE simulation particles from N21 are overlaid in gold, and Sagittarius simulation particles from Vasiliev et al. (2021) in green. Gray regions mask out the main survey selection functions: the Galactic latitude cut of $|b| > 20°$, and the southern declination limit of the underlying spectroscopic catalogs. A simple selection of $v_{\mathrm{t},\,\phi_1} > 0$ isolates presumed members of the GSE debris. In the bottom row of panels, we only show observed and simulated stars that satisfy this criterion, in the transverse (relative to the stream track) proper motion, distance, and line-of-sight velocity planes. For reference, the mean parameters of the apocentric overdensities followed up with MIKE are overlaid (see Section 3).

shown without the Sagittarius L_Y cut applied, to establish the clear difference between the GSE and Sagittarius in our data. We show simulation particles of the GSE merger from N21, along with simulated Sagittarius stars from Vasiliev et al. (2021). We select retrograde 6D giants that lie within $\phi_2 \leqslant 35°$ of the great circle frame—in practice, this spatial cut removes only eight field retrograde stars that lie elsewhere on the sky. We apply a further purity cut of $v_{\mathrm{t},\,\phi_1} > 0$ to select stars that move along the great circle—this removes another three stars, leaving 49 stars in the distant retrograde sample. The stars that fail this cut are likely field halo stars that happen to be retrograde, or genuine stream stars with large proper motion errors. Their XP metallicity distribution is peaked at [Fe/H] ≈ -1.2, consistent with the field halo at these distances (Conroy et al. 2019a). In the bottom panels of Figure 7 we only show stars that satisfy these criteria.

The top right panel of Figure 7 shows the tangential velocity along the ϕ_1 coordinate, emphasizing how different the proper motions of the retrograde giants are from Sagittarius, despite lying in a similar on-sky plane. Although there is generally good agreement between our data and the N21 simulations in all these panels, the distribution of ϕ_2 tangential velocities is hotter in the data than the simulations (bottom left panel). This could reflect some perturbative process not considered in the simulations, like the growing Milky Way disk or the influence of Sagittarius and the Large Magellanic Cloud (e.g., Law & Majewski 2010b; Gómez et al. 2015; Erkal et al. 2016; Koposov et al. 2023). The N21 simulations predict distant $d \gtrsim 50$ kpc debris at two location along this stream track, both of which we identify in the data as the OVO (MIKE-N, $\phi_1 \sim 0°$) and Pisces Overdensity (MIKE-S, $\phi_1 \sim 130°$), respectively (bottom middle panel). The disordered but net $\approx$0 km s^{-1} Galactocentric radial velocities are typical of "shells" of merger debris in simulations (bottom right panel; e.g., Hernquist & Spergel 1992; Pop et al. 2018; Dong-Páez et al. 2022).

We finally explore this all-sky retrograde debris in chemistry. We utilize the subset of retrograde 6D giants shown in Figure 6 that have data from H3 and SEGUE. Both the H3 and SEGUE data sets were fitted using the `MINESweeper` routine to derive [Fe/H] and [α/Fe], and therefore share the same abundance scale (more details are given in Cargile et al. 2020). We illustrate this chemical space in Figure 8. The background log-scaled histogram shows all stars in the H3 survey, and the golden points show GSE giants selected from H3 using the cuts of Naidu et al. (2020). The retrograde giants we identify in this work match the GSE chemical sequence, clustering around its locus. We note that much of the outer halo shares a similar locus, perhaps in part because the GSE itself forms much of the diffuse outer halo. There are a few retrograde stars off the GSE track with low [Fe/H] and low [α/Fe], plausibly stars from past minor mergers with smaller dwarf galaxies (e.g., Cohen & Huang 2009, 2010).

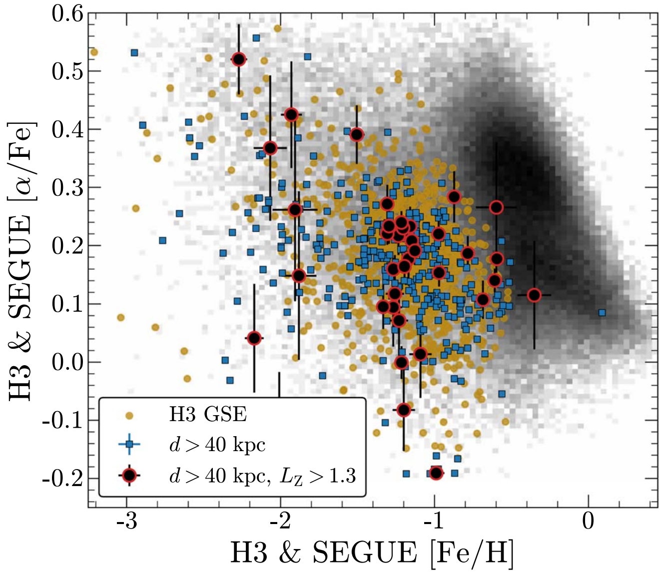

Figure 8. Distribution of the [Fe/H] vs. [α/Fe] abundances among the distant (blue squares) and retrograde (black and red circles) stars in our 6D giants data set. We use stars with spectra from the H3 Survey and the SEGUE survey; both have been fitted using the techniques of Cargile et al. (2020) and lie on a similar abundance scale. For reference, we overlay in gold H3 GSE giants selected following Naidu et al. (2020), with the log-scaled background histogram showing all stars in the H3 Survey.

4.3. Metallicity Gradient of GSE's Outer Disk

The distant GSE debris identified here are expected to contain the earliest-stripped stars from the outer regions of the GSE progenitor, since they retain the progenitor's large initial angular momentum prior to radialization. This correspondence between the GSE disk radius and present-day angular momenta can be used to trace observed stars back to their predicted location in the simulated GSE disk. We query the $z = 0$ snapshots from N21 to select stars similar to our MIKE targets in Galactocentric coordinates, and trace them back to their locations in the intact $z = 2$ GSE progenitor. The resulting (cumulative) radial distributions are shown in the top panel of Figure 9. We also show the corresponding distributions for simulation particles selected following the inner GSE and Arjuna selections in the H3 Survey. Clearly, these populations originate from different radial regions of the GSE progenitor. Following N21, we can leverage this effect to measure the metallicity gradient of the GSE progenitor out to three times its half-mass radius.

For the GSE and Arjuna metallicities, we utilize the H3 Survey measurements from N21. For the MIKE-N and MIKE-S stars, we use our Gaia DR3 XP metallicities (Section 2) since they were trained on H3 data and should lie on a comparable metallicity scale, whereas the CaT metallicities are systematically offset by ≈0.1 dex (more metal poor) compared to XP. Finally, we include the all-sky retrograde debris beyond 40 kpc described in Section 4.2, again using the XP metallicities for consistency. We select correspondingly distant and retrograde particles from the N21 simulation, after applying the on-sky survey selection function shown in Figure 6.

For each sample described above, we measure the median (spherical) Galactocentric radius in the simulated GSE progenitor $r_{\rm GSE}$, as well as the median observed metallicity with bootstrapped uncertainties. We display the resulting metallicity gradient in the bottom panel of Figure 9, along with a linear fit that accounts for the heteroskedastic metallicity measurements. We measure a gradient of $d[\mathrm{Fe/H}]/dr = -0.02 \pm 0.01$ dex kpc^{-1}, or $d\,[\mathrm{Fe/H}]/dr_{50} = -0.06 \pm 0.02$ dex r_{50}^{-1} when normalizing to the simulated GSE half-mass radius of ≈2.8 kpc.

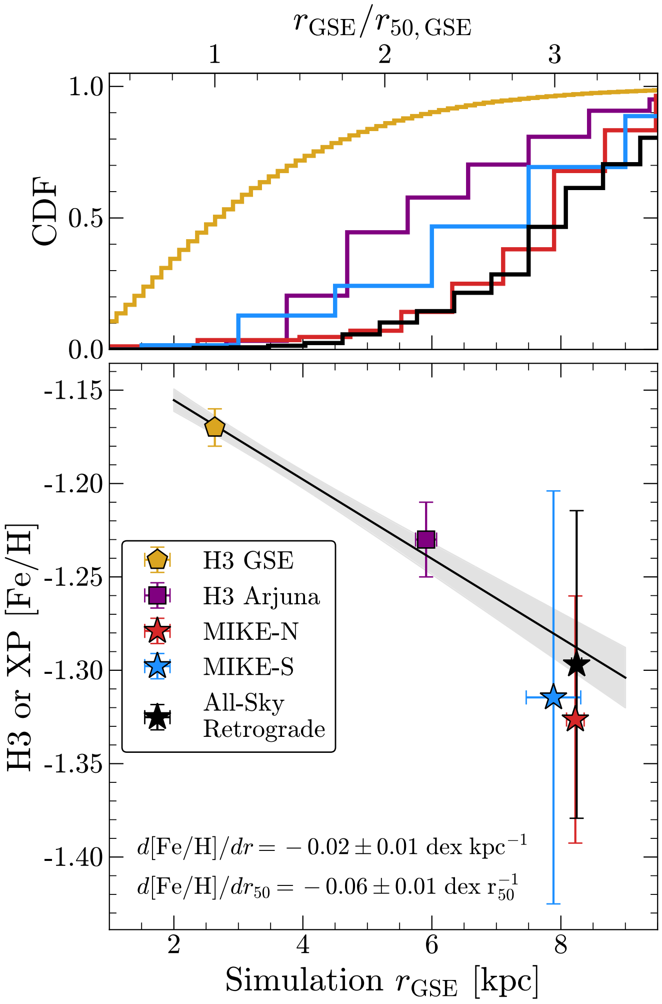

Figure 9. Measuring the metallicity gradient of the GSE progenitor to three times its half-mass radius. We use the simulations of N21 to map the present-day kinematics of the GSE debris to their initial radii within the progenitor. Top: cumulative radial distribution of simulated stars in the $z = 2$ GSE progenitor, selected to match the observed tracers at $z = 0$ kinematically: H3 GSE in gold, H3 Arjuna in purple, and our northern and southern MIKE targets in red and blue, respectively. Bottom: median observed metallicity vs. median simulated GSE galactocentric radius for each population. We fit this metallicity gradient with a linear model and display the best-fit parameters in radial and half-mass radius (r_{50}) coordinates.

The fit is primarily driven by the high-precision H3 data points, but the outer debris presented here are entirely consistent with the inferred negative metallicity gradient. Our conclusions are qualitatively unchanged if we use the MIKE CaT metallicities instead, but they are offset ≈0.1 dex lower than the XP metallicities and would correspondingly lead to a slight tension with the H3-extrapolated linear trend. We emphasize that these uncertainties are purely statistical, and do not account for the (substantial) systematic uncertainty mapping these populations to $r_{\rm GSE}$ via the N21 N-body simulation.

The distant debris presented here probe the very outer disk of the GSE progenitor, and it is reassuring that the metallicity gradient inferred by N21 extrapolates well into this regime. This is a relatively shallow gradient compared to intact dwarf galaxies around the Milky Way (Kirby et al. 2011), supporting the picture that metallicity gradients steepen over cosmic time (e.g., Curti et al. 2020; Sharda et al. 2021; Tissera et al. 2022). We note that if the proposed Sequoia merger (Myeong et al. 2019) is instead a metal-poor and retrograde tail of the GSE merger itself (e.g., Amarante et al. 2022; Horta et al. 2023), then the implied metallicity gradient would be about twice as steep as that measured here (Limberg et al. 2022).

5. Discussion

We have assembled a sample of luminous red giant stars out to 100 kpc and discovered a large population of retrograde debris that we argue represent the most distant echoes of the GSE merger. We first established that the OVO contains predominantly retrograde stars (Figure 4), and found a corresponding retrograde stellar population in the Southern Hemisphere near the previously identified Pisces Overdensity. These structures match the predictions of early-stripped debris piling up near their apocenters, and reproduce two key aspects of the simulations—retrograde kinematics, and a northern overdensity that is ≈30% further than the southern one. We combined our data with the simulations from N21 to map these populations back to their locations in the GSE progenitor's stellar disk, and measured a negative metallicity gradient in this $z \approx 2$ accreted galaxy out to three half-mass radii that is consistent with past measurements from the H3 Survey.

Searching for more distant retrograde stars in the broader sample of giants, we find that the majority ($\gtrsim$80%) of retrograde stars beyond 40 kpc coherently lie along a stream-like track that is well fit by a great circle on the sky (Figure 6). These stars can be cleanly differentiated from cospatial Sagittarius Stream stars based on their kinematics (Figures 6 and 7), and appear chemically consistent with the GSE (Figure 8). A truly all-sky picture evades us due to the lack of spectroscopic data in the Southern celestial Hemisphere. Future spectroscopy of the distant halo in the Southern Hemisphere (e.g., with the Sloan Digital Sky Survey, SDSS-V; Kollmeier et al. 2017) will help fill in this missing portion of the sky.

We summarize the Galactocentric distribution of the various structures described in this work in Figure 10, along with the median orbits of the MIKE-N and MIKE-S sample. The top panels show the shape of inner GSE debris in H3 Survey data (Han et al. 2022; blue), along with a scaled-up version rotated to match the orientation of the MIKE-N and MIKE-S stars (red). These panels illustrate how the 60–90 kpc debris presented in this work relate to the previously identified GSE apocenters that form the 15 to 20 kpc inner OVO and HAC. There is an ≈45° offset between the inner and outer overdensities along two axes. This is consistent with the N21 simulations, in which the inner and outer apocenters are misaligned by up to ≈50° in the x–y plane, due to the sharp radialization of the satellite over time. These four overdensities strongly constrain the infalling trajectory of the GSE progenitor. A natural next step would be to simulate the GSE merger self-consistently to identify a configuration that reproduces the kinematic qualities of the inner halo, along with the spatial orientation of these four overdensities.

5.1. The Emerging Picture of the GSE Merger

In the merger simulations of N21, the GSE progenitor arrived on a tilted and retrograde trajectory before rapidly radializing as it merged with the Milky Way (see also Bignone et al. 2019; Amarante et al. 2022; Vasiliev et al. 2022). The retrograde orientation of the merger was required by N21 to reproduce the kinematics of Arjuna, the population of metal-rich retrograde stars prominently seen in the H3 Survey (Naidu et al. 2020). In this work, we have discovered coherent and relatively metal-rich retrograde debris in the outer halo beyond $\gtrsim$50 kpc, which are reasonably consistent with predictions from the N21 simulations. Our findings beyond 50 kpc match the spatial constraints of the halo's shape at closer distances—specifically that the bulk of the halo is oriented along two preferred octants that contain the inner VO and the HAC (Figure 10; Iorio & Belokurov 2019; Han et al. 2022).

The existence of a significant population of GSE debris at large $r_{\rm Gal}$ has been a generic prediction of simulations of this merger, but the mass and kinematics of this population strongly depend on the assumed configuration. For example, if one invokes an initially radial merger to explain the predominantly radial inner GSE stars, then the remnant could fling a significant fraction of its mass to large distances as it merges (e.g., Elias et al. 2020). However, both N-body simulations and analytic calculations have shown that a merger as massive as the GSE would self-radialize on short timescales, eventually creating inner debris with low angular momenta for a wide range of initial merger angular momenta (Amorisco 2017; N21; Vasiliev et al. 2022). In more gradual merger scenarios, a smaller fraction of accreted stars would be deposited at large distances, and they would retain more angular momenta. It is challenging to make quantitative conclusions with our present data given the complex selection functions of the underlying surveys, as well as the use of kinematics to define the distant GSE population in the first place. Regardless, the presence of such a prominent population of retrograde debris in the outer halo leads us to favor the latter merger scenario, in which a retrograde GSE progenitor was gradually stripped of stars that produce the echoes we see beyond $d \gtrsim 50$ kpc. At closer distances, this population transitions into the phase-mixed Arjuna stars, and finally the radialized bulk of GSE debris that dominate the inner stellar halo (Donlon et al. 2020; Naidu et al. 2020).

Our work has presented evidence for distant and early-stripped retrograde GSE debris in the outer halo beyond 40 kpc. These kinematics strongly suggest that the orientation of the GSE merger was retrograde, matching the results from N21, and the presence of the retrograde Arjuna population in the H3 Survey from 15 to 30 kpc. Conversely, Belokurov et al. (2023) argue for a prograde merger orientation based on the slight prograde tilt of GSE stars in their Gaia DR3 RVS data set, which is primarily limited within $\lesssim$15 kpc. In the absence of $[\alpha/\mathrm{Fe}]$ information, the RVS sample could be contaminated by prograde stars from the in situ halo population (e.g., Bonaca et al. 2017; Belokurov et al. 2020; Bonaca et al. 2020). However, a more subtle prograde tilt is also seen in the APOGEE DR17 data set once the in situ halo is filtered out via $[\alpha/\mathrm{Fe}]$ (V. Belokurov, private communication; Majewski et al. 2017; Abdurro'uf et al. 2022). A plausible resolution to this discrepancy is that the bulk of retrograde Arjuna stars lie beyond $d \gtrsim 15$ kpc, whereas the RVS and APOGEE samples primarily contain more nearby stars. Therefore, the earlier-stripped retrograde component could be mostly absent from these nearer data sets, while appearing prominently in the more distant H3 Survey, and in this present work.

Any conclusions linking present-day merger debris to the original configuration of the merger are complicated by the

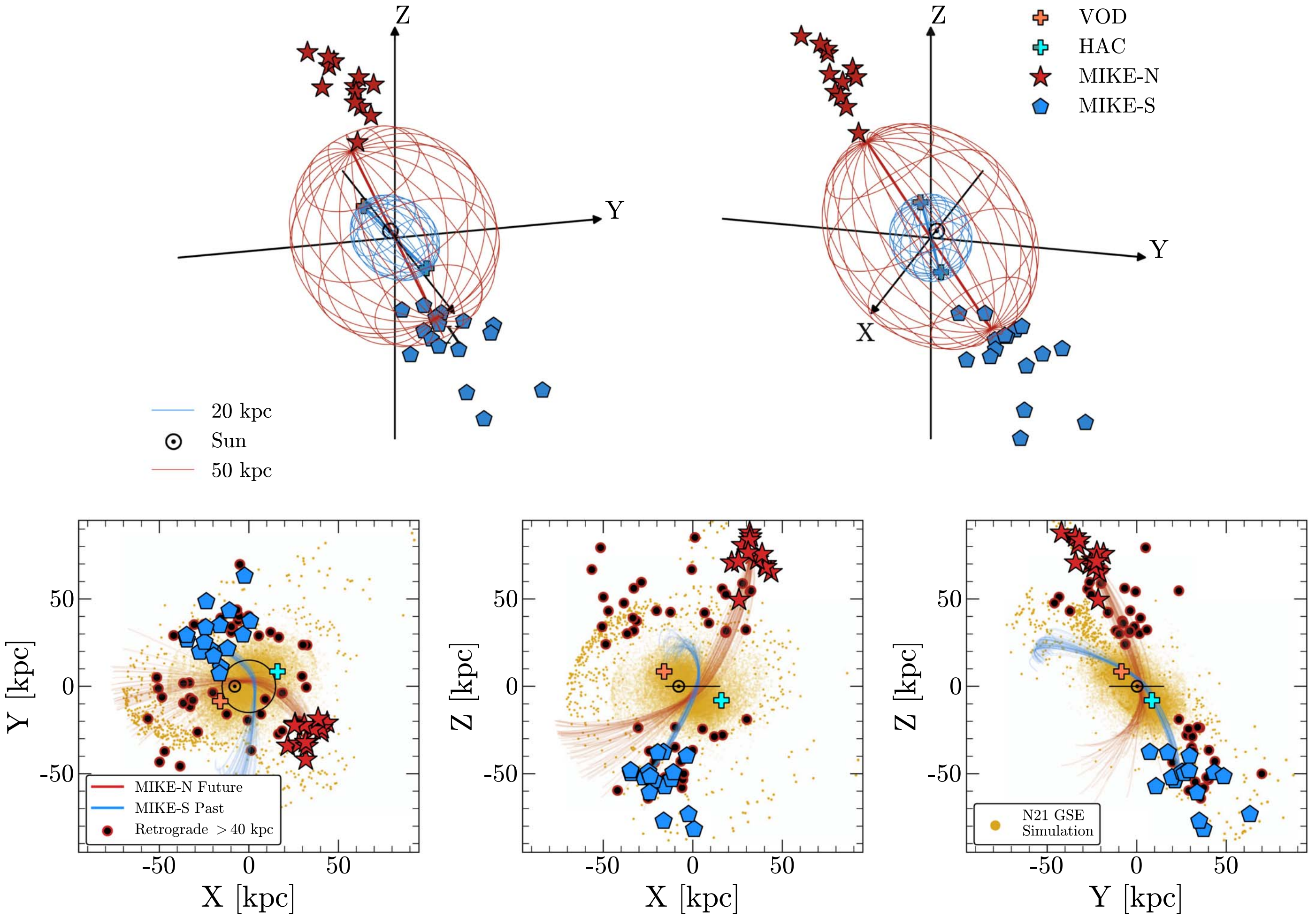

Figure 10. Galactocentric distribution of the structures described in this work. The top panels show two 3D projections of the data, whereas the bottom panels are 2D projections along each axis. The previously identified HAC and (inner) VO are shown with plus symbols using the RRL star locations from Simion et al. (2019). In the top panels we show in blue the shape of the inner GSE debris fitted to H3 Survey data by Han et al. (2022), evaluated at 20 kpc. Our MIKE-N sample in the OVO and MIKE-S sample in the Pisces Overdensity are overlaid using the adopted MIKE spectroscopic distances. The red ellipsoid in the top panels is a scaled-up version of the Han et al. (2022) profile evaluated at 50 kpc, rotated to align with the MIKE-N and MIKE-S stars. In the bottom panels we also show retrograde GSE "stream" members from the 6D Gaia XP giant sample (see Figures 6 and 7). GSE simulation particles from N21 at $z = 0$ are shown in gold, with particles beyond 50 kpc emphasized. 100 realizations of the mean future (past) orbits of the MIKE-N (MIKE-S) stars are overlaid (see Section 3.2 and Figure 4).

precession of the Milky Way disk, which would shift the angular momentum vector of the galaxy (e.g., Dillamore et al. 2022; Dodge et al. 2023). N21 did not account for disk precession in their angular momentum calculations. However, they also did not model the growing of the Milky Way disk since $z \approx 2$. It is reasonable to expect that a growing disk could suppress the degree of precession, preserving the linkage between the original and present-day angular momenta. The fact that the distant debris shown here closely match the N21 simulations in angular momentum—despite neglecting the effect of precession—could be a hint that the Milky Way disk has only weakly precessed since $z \approx 2$. A more comprehensive test would be to simulate the GSE merger self-consistently with a growing disk, and track the evolving angular momenta of the resulting debris.

5.2. An Outer Halo in Disequilibrium

A broader implication of this work is apparent in our all-sky maps of the distant halo (Figure 2). The Milky Way's outer halo contains significant substructure, and is in fact dominated by it. Due to the prominence of these disequilibrium structures, any efforts to measure the Milky Way's properties in the outer halo—from its mass to the perturbative response of its dark matter halo (e.g., Garavito-Camargo et al. 2019, 2021; Shen et al. 2022)—will require more sophisticated and time-dependent modeling (e.g., Vasiliev et al. 2021; Koposov et al. 2023; Lilleengen et al. 2023).

Four overdensities overwhelm our maps beyond 60 kpc: the Sagittarius Stream, the OVO, the Pisces Overdensity, and the elongated Pisces Plume flowing from the Magellanic Clouds. The former three structures are clearly visible via RRL stars, whereas the latter is most prominent in the RGB maps. In this work we have argued that both the OVO and at least some part of the Pisces Overdensity can be linked to the GSE merger; the origin of the Pisces Plume remains more uncertain, particularly to what extent it comprises Magellanic debris or the dynamical friction wake of the Large Magellanic Cloud. We have shown here how precise 6D kinematics and chemistry of even a handful of members can offer key links to the origins of a structure.

6. Conclusions

We have constructed an all-sky sample of luminous red giants out to 100 kpc with metallicities from Gaia DR3 XP spectra, and augmented it with radial velocities from public surveys as well as follow-up spectroscopy. The key conclusions from our work are as follows:

1. The outer halo beyond ≈40 kpc is richly structured, with four prominent overdensities dominating the sky: the Sagittarius Stream, OVO, Pisces Overdensity, and Pisces Plume (Figure 2).
2. Using follow-up MIKE spectroscopy of the OVO and Pisces Overdensity, we find both to be relatively metal rich ($[\mathrm{Fe/H}] \approx -1.3$)—similar to the bulk of the stellar halo at these distances—and orbiting significantly retrograde relative to the Milky Way disk. We consequently argue that both of these overdensities represent apocentric pileup of debris from the GSE dwarf galaxy, matching key predictions from simulations of the merger (Figure 4).
3. Extending our search across the sky, we find evidence for a vast stream of retrograde stars encircling the Milky Way between 40 and 100 kpc, in the same plane as the Sagittarius Stream albeit moving in the opposite direction (Figure 6). Together with the OVO and Pisces Overdensity, we identify these stars as the earliest-stripped debris from the GSE merger.
4. We use our sample to measure the metallicity gradient in the $z \approx 2$ GSE progenitor out to the edge of its stellar disk, exploiting the link between present-day angular momentum and progenitor galactocentric radius. Although the systematic and statistical uncertainties are large, we find a negative metallicity gradient $d[\mathrm{Fe/H}]/dr_{50} = -0.06 \pm 0.02$ dex r_{50}^{-1}, consistent with previous studies (Figure 9).

Our discovery of coherent retrograde debris beyond 40 kpc argues for an initially retrograde orbit of the GSE progenitor, a matter of debate in the current literature. The location and kinematics of the stars presented here can be used to constrain further the orbit of the merging progenitor at early times, building toward a precise picture of the last major merger that formed the majority of the Milky Way's stellar halo. More broadly, the methods presented here to identify distant RGB stars should enable a spectroscopic census of the outer halo in 6D, finally unmasking the patchwork of accreted structure that enshrouds our galaxy.

Acknowledgments

We thank the referee for constructive feedback that significantly improved the manuscript. V.C. gratefully acknowledges a Peirce Fellowship from Harvard University. We thank Morgan Fouesneau, Rene Andrae, David W. Hogg, Tom Donlon, Guilherme Limberg, and Will Cerny for insightful conversations, and Vasily Belokurov for detailed feedback. We acknowledge Kevin Schlaufman for inspiring the "ECHOS" in the title of this work. We are grateful to the staff at Las Campanas Observatory—including Yuri Beletsky, Carla Fuentes, Jorge Araya, Hugo Rivera, Alberto Pastén, Roger Leiton, Matías Díaz, and Carlos Contreras—for their invaluable assistance. C.C. and P.C. acknowledge support from NSF grant NSF AST-2107253. Support for this work was provided by NASA through the NASA Hubble Fellowship grant HST-HF2-51515.001-A awarded by the Space Telescope Science Institute, which is operated by the Association of Universities for Research in Astronomy, Incorporated, under NASA contract NAS5-26555.

This work has made use of data from the European Space Agency (ESA) mission Gaia (https://www.cosmos.esa.int/gaia), processed by the Gaia Data Processing and Analysis Consortium (DPAC, https://www.cosmos.esa.int/web/gaia/dpac/consortium). Funding for the DPAC has been provided by national institutions, in particular the institutions participating in the Gaia Multilateral Agreement. Funding for the Sloan Digital Sky Survey IV has been provided by the Alfred P. Sloan Foundation, the U.S. Department of Energy Office of Science, and the Participating Institutions. Guoshoujing Telescope (the Large Sky Area Multi-Object Fiber Spectroscopic Telescope; LAMOST) is a National Major Scientific Project built by the Chinese Academy of Sciences. Funding for the project has been provided by the National Development and Reform Commission. LAMOST is operated and managed by the National Astronomical Observatories, Chinese Academy of Sciences. This research has made extensive use of NASA's Astrophysics Data System Bibliographic Services. This publication makes use of data products from the Wide-field Infrared Survey Explorer, which is a joint project of the University of California, Los Angeles, and the Jet Propulsion Laboratory/California Institute of Technology, funded by the National Aeronautics and Space Administration.

Facilities: Gaia, WISE, Magellan:Clay (MIKE), MMT (Hectochelle), Sloan, LAMOST.

Software: `numpy` (Harris et al. 2020), `scipy` (Virtanen et al. 2020), `matplotlib` (Hunter 2007), `gala` (Price-Whelan 2017; Price-Whelan et al. 2020) `MINESweeper` (Cargile et al. 2020).

Appendix
MIKE Spectroscopy

In Table 1 we list the stars with follow-up MIKE spectroscopy from the MIKE-N (OVO) and MIKE-S (Pisces Overdensity) samples presented in this work. We provide the CaT metallicities as estimated using the calibration of Carrera et al. (2013).

Table 1
Stars with Follow-up Spectroscopy from Magellan/MIKE

Gaia Source ID EDR3	R.A. (deg)	Decl. (deg)	G (mag)	MIKE $v_{r,h}$ (km s^{-1})	MIKE [Fe/H] (dex)
3618701644156259840	208.208	−8.921	17.1	−52.2	−1.5
3619451541150749696	210.237	−7.164	16.9	43.5	−1.1
3629830484239963392	197.219	−5.127	17.1	56.5	−1.2
3635542382722531072	198.599	−5.704	17.1	58.1	−1.3
3636560530489773312	200.267	−3.084	16.8	2.5	−1.2
3637038882471985536	201.534	−3.407	17.3	101.3	−1.3
3637178009347886976	202.26	−2.88	16.9	−1.1	−1.5
3639801478451745152	214.924	−7.219	17.1	−38.2	−1.8
3640443314069314432	211.555	−6.825	17.0	−23.5	−1.4
3656976434192873088	208.364	−4.257	16.6	110.6	−1.4
3659398314711482624	211.511	−1.183	17.4	75.5	−1.3
3662283261424032256	206.258	−0.294	16.6	−8.2	−1.3
3662686709176714752	204.023	−0.192	17.1	18.1	−1.2
2372535196962774912	13.193	−14.292	16.4	−36.8	−1.1
2431365283865625472	4.032	−6.307	16.7	−0.2	−1.3
2438768536173626752	354.67	−8.787	16.9	−55.2	−2.4
2454879993588592512	18.87	−15.281	16.1	76.9	−1.2
2469715257305762560	17.086	−11.468	16.9	−51.3	−1.2
2529777385642667136	12.537	−2.1	16.8	−87.6	−1.3
2534734362017687680	18.063	0.101	16.3	−118.7	−1.3
2540409830586618240	4.513	−3.509	17.0	−0.7	−1.6
2549636867743405952	12.98	1.578	16.9	29.3	−1.1
2552533462406653696	12.949	4.514	16.3	13.4	−2.2
2554005502317914112	8.786	4.096	16.7	−70.6	−1.8
2578800279797928576	19.916	9.139	16.3	−159.8	−1.2
2583539312352584960	18.82	11.716	15.9	−36.6	−2.2
2657602587398571904	348.964	1.815	17.0	−180.6	−1.6
2664334794016300288	348.748	6.481	17.2	−121.0	−1.2
2761521550212895232	353.562	9.753	16.9	−8.9	−0.8
2772570443776800384	1.776	16.206	16.1	−97.3	−1.1

ORCID iDs

Vedant Chandra https://orcid.org/0000-0002-0572-8012
Rohan P. Naidu https://orcid.org/0000-0003-3997-5705
Charlie Conroy https://orcid.org/0000-0002-1590-8551
Alexander P. Ji https://orcid.org/0000-0002-4863-8842
Hans-Walter Rix https://orcid.org/0000-0003-4996-9069
Ana Bonaca https://orcid.org/0000-0002-7846-9787
Phillip A. Cargile https://orcid.org/0000-0002-1617-8917
Jiwon Jesse Han https://orcid.org/0000-0002-6800-5778
Benjamin D. Johnson https://orcid.org/0000-0002-9280-7594
Yuan-Sen Ting (丁源森) https://orcid.org/0000-0001-5082-9536
Turner Woody https://orcid.org/0000-0002-0721-6715
Dennis Zaritsky https://orcid.org/0000-0002-5177-727X

References

Abdurro'uf, Accetta, K., Aerts, C., et al. 2022, ApJS, 259, 35
Alam, S., Albareti, F. D., Allende Prieto, C., et al. 2015, ApJS, 219, 12
Amarante, J. A. S., Debattista, V. P., Beraldo E Silva, L., Laporte, C. F. P., & Deg, N. 2022, ApJ, 937, 12
Amorisco, N. C. 2017, MNRAS, 464, 2882
Bailer-Jones, C. A. L. 2004, A&A, 419, 385
Belokurov, V., Deason, A. J., Erkal, D., et al. 2019, MNRAS, 488, L47
Belokurov, V., Erkal, D., Evans, N. W., Koposov, S. E., & Deason, A. J. 2018, MNRAS, 478, 611
Belokurov, V., Evans, N. W., Bell, E. F., et al. 2007, ApJL, 657, L89
Belokurov, V., Sanders, J. L., Fattahi, A., et al. 2020, MNRAS, 494, 3880
Belokurov, V., Vasiliev, E., Deason, A. J., et al. 2023, MNRAS, 518, 6200
Bennett, M., & Bovy, J. 2019, MNRAS, 482, 1417
Bernstein, R., Shectman, S. A., Gunnels, S. M., Mochnacki, S., & Athey, A. E. 2003, Proc. SPIE, 4841, 1694
Besla, G., Hernquist, L., & Loeb, A. 2013, MNRAS, 428, 2342
Bignone, L. A., Helmi, A., & Tissera, P. B. 2019, ApJL, 883, L5
Bonaca, A., Conroy, C., Cargile, P. A., et al. 2020, ApJL, 897, L18
Bonaca, A., Conroy, C., Wetzel, A., Hopkins, P. F., & Kereš, D. 2017, ApJ, 845, 101
Bonaca, A., Geha, M., & Kallivayalil, N. 2012, ApJL, 760, L6
Brown, A. G., Vallenari, A., Prusti, T., et al. 2021, A&A, 649, 1
Cargile, P. A., Conroy, C., Johnson, B. D., et al. 2020, ApJ, 900, 28
Carlin, J. L., Yam, W., Casetti-Dinescu, D. I., et al. 2012, ApJ, 753, 145
Carrera, R., Pancino, E., Gallart, C., & del Pino, A. 2013, MNRAS, 434, 1681
Chambers, K. C., Magnier, E. A., Metcalfe, N., et al. 2016, arXiv:1612.05560
Choi, J., Dotter, A., Conroy, C., et al. 2016, ApJ, 823, 102
Clementini, G., Ripepi, V., Garofalo, A., et al. 2022, arXiv:2206.06278
Cohen, J. G., & Huang, W. 2009, ApJ, 701, 1053
Cohen, J. G., & Huang, W. 2010, ApJ, 719, 931
Conroy, C., Bonaca, A., Naidu, R. P., et al. 2018, ApJL, 861, L16
Conroy, C., Naidu, R. P., Garavito-Camargo, N., et al. 2021, Natur, 592, 534
Conroy, C., Naidu, R. P., Zaritsky, D., et al. 2019a, ApJ, 887, 237
Conroy, C., Bonaca, A., Cargile, P., et al. 2019b, ApJ, 883, 107
Cui, X.-Q., Zhao, Y.-H., Chu, Y.-Q., et al. 2012, RAA, 12, 1197
Curti, M., Maiolino, R., Cirasuolo, M., et al. 2020, MNRAS, 492, 821
Das, P., & Binney, J. 2016, MNRAS, 460, 1725
Das, P., Hawkins, K., & Jofré, P. 2020, MNRAS, 493, 5195
De Angeli, F., Weiler, M., Montegriffo, P., et al. 2023, A&A, 674, A2
Deason, A. J., Belokurov, V., Evans, N. W., & Johnston, K. V. 2013, ApJ, 763, 113
Dillamore, A. M., Belokurov, V., Font, A. S., & McCarthy, I. G. 2022, MNRAS, 513, 1867
Dodge, B. C., Slone, O., Lisanti, M., & Cohen, T. 2023, MNRAS, 518, 2870
Dong-Páez, C. A., Vasiliev, E., & Evans, N. W. 2022, MNRAS, 510, 230

Donlon, T., I, Newberg, H. J., Sanderson, R., & Widrow, L. M. 2020, ApJ, 902, 119

Donlon, T., I, Newberg, H. J., Weiss, J., Amy, P., & Thompson, J. 2019, ApJ, 886, 76

Drimmel, R., & Poggio, E. 2018, RNAAS, 2, 210

Eisenstein, D. J., Weinberg, D. H., Agol, E., et al. 2011, AJ, 142, 72

Elias, L. M., Sales, L. V., Helmi, A., & Hernquist, L. 2020, MNRAS, 495, 29

Erkal, D., Belokurov, V., Laporte, C. F., et al. 2019, MNRAS, 487, 2685

Erkal, D., Sanders, J. L., & Belokurov, V. 2016, MNRAS, 461, 1590

Fattahi, A., Belokurov, V., Deason, A. J., et al. 2019, MNRAS, 484, 4471

Feuillet, D. K., Feltzing, S., Sahlholdt, C. L., & Casagrande, L. 2020, MNRAS, 497, 109

Gaia Collaboration, Vallenari, A., Brown, A. G. A., et al. 2022a, arXiv:2208.00211

Gaia Collaboration, Montegriffo, P., Bellazzini, M., et al. 2022b, arXiv:2206.06215

GRAVITY Collaboration, Abuter, R., Amorim, A., et al. 2018, A&A, 615, L15

Gallart, C., Bernard, E. J., Brook, C. B., et al. 2019, NatAs, 3, 932

Garavito-Camargo, N., Besla, G., Laporte, C. F. P., et al. 2019, ApJ, 884, 51

Garavito-Camargo, N., Besla, G., Laporte, C. F. P., et al. 2021, ApJ, 919, 109

Gómez, F. A., Besla, G., Carpintero, D. D., et al. 2015, ApJ, 802, 128

Han, J. J., Conroy, C., Johnson, B. D., et al. 2022, AJ, 164, 249

Harris, C. R., Millman, K. J., van der Walt, S. J., et al. 2020, Natur, 585, 357

Hasselquist, S., Zasowski, G., Feuillet, D. K., et al. 2020, ApJ, 901, 109

Haywood, M., Di Matteo, P., Lehnert, M. D., et al. 2018, ApJ, 863, 113

Helmi, A., Babusiaux, C., Koppelman, H. H., et al. 2018, Natur, 563, 85

Hernquist, L., & Spergel, D. N. 1992, ApJL, 399, L117

Horta, D., Schiavon, R. P., Mackereth, J. T., et al. 2023, MNRAS, 520, 5671

Hunter, J. D. 2007, CSE, 9, 90

Iorio, G., & Belokurov, V. 2019, MNRAS, 482, 3868

Iorio, G., Belokurov, V., Erkal, D., et al. 2018, MNRAS, 474, 2142

Johnson, B. D., Conroy, C., Naidu, R. P., et al. 2020, ApJ, 900, 103

Johnson, J. W., Conroy, C., Johnson, B. D., et al. 2022, arXiv:2210.01816

Jurić, M., Ivezić, Ž., Brooks, A., et al. 2008, ApJ, 673, 864

Katz, D., Sartoretti, P., Guerrier, A., et al. 2022, arXiv:2206.05902

Kelson, D. 2003, PASP, 115, 688

Kirby, E. N., Lanfranchi, G. A., Simon, J. D., Cohen, J. G., & Guhathakurta, P. 2011, ApJ, 727, 78

Kollmeier, J. A., Gould, A., Shectman, S., et al. 2009, ApJL, 705, L158

Kollmeier, J. A., Zasowski, G., Rix, H.-W., et al. 2017, arXiv:1711.03234

Koposov, S. E., Erkal, D., Li, T. S., et al. 2023, MNRAS, 521, 4936

Lancaster, L., Koposov, S. E., Belokurov, V., Evans, N. W., & Deason, A. J. 2019, MNRAS, 486, 378

Law, D. R., & Majewski, S. R. 2010a, ApJ, 714, 229

Law, D. R., & Majewski, S. R. 2010b, ApJ, 718, 1128

Lee, Y. S., Beers, T. C., Sivarani, T., et al. 2008, AJ, 136, 2022

Li, T. S., Balbinot, E., Mondrik, N., et al. 2016, ApJ, 817, 135

Lilleengen, S., Petersen, M. S., Erkal, D., et al. 2023, MNRAS, 518, 774

Limberg, G., Souza, S. O., Pérez-Villegas, A., et al. 2022, ApJ, 935, 109

Lindegren, L., Klioner, S. A., Hernández, J., et al. 2021, A&A, 649, A2

Lucchini, S., D'Onghia, E., Fox, A. J., D'Onghia, E., & Fox, A. J. 2021, ApJL, 921, L36

Mackereth, J. T., Schiavon, R. P., Pfeffer, J., et al. 2019, MNRAS, 482, 3426

Mainzer, A., Bauer, J., Cutri, R. M., et al. 2014, ApJ, 792, 30

Majewski, S. R., Schiavon, R. P., Frinchaboy, P. M., et al. 2017, AJ, 154, 94

Majewski, S. R., Skrutskie, M. F., Weinberg, M. D., & Ostheimer, J. C. 2003, ApJ, 599, 1082

Marín-Franch, A., Chueca, S., Moles, M., et al. 2012, Proc. SPIE, 8450, 84503S

Montegriffo, P., De Angeli, F., Andrae, R., et al. 2023, A&A, 674, A3

Myeong, G. C., Vasiliev, E., Iorio, G., Evans, N. W., & Belokurov, V. 2019, MNRAS, 1247, 1235

Naidu, R. P., Conroy, C., Bonaca, A., et al. 2020, ApJ, 901, 48

Naidu, R. P., Conroy, C., Bonaca, A., et al. 2021, ApJ, 923, 92

Newberg, H. J., Yanny, B., & Willett, B. A. 2009, ApJ, 700, 10

Nidever, D. L., Majewski, S. R., & Butler Burton, W. 2008, ApJ, 679, 432

Nie, J. D., Smith, M. C., Belokurov, V., et al. 2015, ApJ, 810, 153

Pedregosa, F., Varoquaux, G., Gramfort, A., et al. 2011, JMLR, 12, 2825

Perottoni, H. D., Limberg, G., Amarante, J. A. S., et al. 2022, ApJL, 936, L2

Pop, A.-R., Pillepich, A., Amorisco, N. C., & Hernquist, L. 2018, MNRAS, 480, 1715

Price-Whelan, A., Sipőcz, B., Lenz, D., et al. 2020, adrn/gala: v1.3, Zenodo, doi:10.5281/zenodo.4159870

Price-Whelan, A. M. 2017, JOSS, 2, 388

Reid, M. J., & Brunthaler, A. 2004, ApJ, 616, 872

Rix, H.-W., Chandra, V., Andrae, R., et al. 2022, ApJ, 941, 45

Ruz-Mieres, D. 2022, gaia-dpci/GaiaXPy: GaiaXPy v1.1.4, Zenodo, doi:10.5281/zenodo.6674521

Schlafly, E. F., & Finkbeiner, D. P. 2011, ApJ, 737, 103

Schlafly, E. F., Meisner, A. M., & Green, G. M. 2019, ApJS, 240, 30

Schlegel, D. J., Finkbeiner, D. P., & Davis, M. 1998, ApJ, 500, 525

Sesar, B., Hernitschek, N., Dierickx, M. I. P., Fardal, M. A., & Rix, H.-W. 2017a, ApJL, 844, L4

Sesar, B., Hernitschek, N., Mitrović, S., et al. 2017b, AJ, 153, 204

Sesar, B., Ivezić, Ž., Lupton, R. H., et al. 2007, AJ, 134, 2236

Sesar, B., Vivas, A. K., Duffau, S., & Živezić, E. 2010, ApJ, 717, 133

Sharda, P., Wisnioski, E., Krumholz, M. R., & Federrath, C. 2021, MNRAS, 506, 1295

Shen, J., Eadie, G. M., Murray, N., et al. 2022, ApJ, 925, 1

Simion, I. T., Belokurov, V., & Koposov, S. E. 2019, MNRAS, 482, 921

Simion, I. T., Belokurov, V., Koposov, S. E., Sheffield, A., & Johnston, K. V. 2018, MNRAS, 476, 3913

Strömgren, B. 1966, ARA&A, 4, 433

Ting, Y.-S., Conroy, C., Rix, H.-W., & Cargile, P. 2019, ApJ, 879, 69

Tissera, P. B., Rosas-Guevara, Y., Sillero, E., et al. 2022, MNRAS, 511, 1667

Vasiliev, E., Belokurov, V., & Erkal, D. 2021, MNRAS, 501, 2279

Vasiliev, E., Belokurov, V., & Evans, N. W. 2022, ApJ, 926, 203

Vincenzo, F., Spitoni, E., Calura, F., et al. 2019, MNRAS, 487, L47

Virtanen, P., Gommers, R., Oliphant, T. E., et al. 2020, NatMe, 17, 261

Watkins, L. L., Evans, N. W., Belokurov, V., et al. 2009, MNRAS, 398, 1757

Xiang, M., Ting, Y.-S., Rix, H.-W., et al. 2019, ApJS, 245, 34

Xue, X. X., Rix, H. W., Ma, Z., et al. 2015, ApJ, 809, 144

Yanny, B., Rockosi, C., Newberg, H. J., et al. 2009, AJ, 137, 4377

Zaritsky, D., Conroy, C., Naidu, R. P., et al. 2020, ApJL, 905, L3

Zhao, G., Zhao, Y.-H., Chu, Y.-Q., Jing, Y.-P., & Deng, L.-C. 2012, RAA, 12, 723